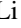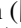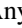# Optical excitation-induced ultrafast amorphization in the Y-Sb-Te alloy system: Insights from real-time time-dependent DFT with molecular dynamics calculations

Li Chen (陈立) [1] Anyang Cui (崔安阳) [1] Ming Li (李明),[1] Shubing Li (李树兵),[1] Shijing Gong (龚士静),[1,*]
Kai Jiang (姜凯) [1] Jinzhong Zhang (张金中),[1] Liangqing Zhu (朱亮清),[1] Liyan Shang (商丽燕),[1] Yawei Li (李亚巍),[1]
Zhigao Hu (胡志高) [1,2,†] and Junhao Chu (褚君浩)[1,2]

[1]*Technical Center for Multifunctional Magneto-Optical Spectroscopy (Shanghai), Engineering Research Center of Nanophotonics & Advanced Instrument (Ministry of Education), Department of Physics, School of Physics and Electronic Science, East China Normal University, Shanghai 200241, China*
[2]*Collaborative Innovation Center of Extreme Optics, Shanxi University, Taiyuan, Shanxi 030006, China*

In general, shortening the laser pulse width can suppress thermal dissipation to allow for sub-picosecond phase change during amorphization, yet there is no consistent evidence for the mechanistic exploration of its ultrafast dynamics at the atomic scale. Herein, a real-time time-dependent density-functional theory molecular dynamic (rt-TDDFT-MD) in a photoexcited fashion is applied to disclose an undetected effect of the experimentally observed Y-Sb-Te amorphization process at elevated temperature. Varying the optical excitation from 2% to 8% of valence electrons during the amorphization process can result in a variety of structures ranging from entire crystalline to amorphied shapes, satisfying the amorphous state at 1.2 ps upon 8% excitation. We conclude that the low concentration of photoexcitation fails to conquer the potential barrier height of Y-Sb-Te for fully facilitating amorphization. The 8% of photoinduced Te-p electrons enhances the massive occupation of Y-dt_{2g} orbitals and creates a flatter potential energy surface, which forces Y-centered motifs to perform dt_{2g}- and e_g- directed transition in the signature bond angle of the rock salt lattice. Thus it can rapidly dissociate the Sb-Te bond and facilitate the ultrafast formation of the amorphous phase. The incorporation of optical interventions drives the lattice to manifest disordered states, as well as allowing for accurate manipulation of the electronic structure to further reduce the time consumed in the amorphization process. The present works pave the way for the design of PCMs-based optoelectronic and microelectronic devices with comprehensive ultrafast response.

I. INTRODUCTION

In the current era of explosive information development, there is a growing obsession with processing-in-memory and new materials that support hardware acceleration [1–4]. In particular, phase-change materials (PCMs) benefit from rapid response between crystalline and amorphous states under moderate electrical and laser pulses, etc. PCMs-based devices take advantage of the contrasting optoelectronic and microelectronic properties between the amorphous and crystalline phases to ensure their application in nonvolatile electrical and optical memories [5–8]. The rapid crystallization kinetics of PCMs can be classified as nucleation-dominated and growth-dominated, both corresponding to ultrafast crystal nucleation and growth rates, respectively, and leading to micro- and nanosized crystals [1,9,10]. As a well-known growth-preferred PCM, the Sb_2Te_3 binary alloy commonly used for optical storage shows a faster crystalline phase change than the nucleation-dominated $Ge_2Sb_2Te_5$ (GST) [11]. Its inherent crystallization advantage in combination with the high index of thermal stability obtained by the doping process

gives it the prospect for a wide range of applications [12–14]. As we know, strong electrical/optical pulses are often used to drive homogeneous thermal phase change in SbTe-based PCMs, which inevitably allow the presence of heat-affected zones leading to less refined areas for processing or modification and deteriorating fatigue properties. Nevertheless, ultrashort pulsed lasers (e.g., femtosecond lasers) can effectively suppress the thermal effects and significantly improve the accuracy of processing and modification, playing a crucial role in the field of micro- and nanoprocessing [15,16].

For example, optical applications based on PCMs have also come under close scrutiny in recent years. Based on the experiments, Chen *et al.* revealed that the femtosecond laser simulated by time-dependent density-functional theory molecular dynamic (TDDFT-MD) can induce the GeTe potential energy surface [001] to change from a single-energy valley to a double-energy one, allowing the Ge and Te therein to move out of phase. It establishes an atomic phase diagram for the rhombic to cubic solid-state phase change [17]. By femtosecond x-ray diffractions (800 nm, 30 fs), Matsubara *et al.* proposed a rattling model in both GeTe and $Ge_2Sb_2Te_5$ crystals at photon energies of about 1.55 eV, with Te maintaining at their original positions and Ge rattling between six equivalent off-center positions of the rhombohedral (r) phase as a result of the excitation [18]. Moreover, for the tuning

———————
*sjgong@ee.ecnu.edu.cn
†zghu@ee.ecnu.edu.cn

of the femtosecond laser itself can decouple the competing unity relationship of fermions and bosons in PCMs at the sub-picosecond scale. Liu *et al.* applied an ultrashort pulsed laser (800 nm, 7 fs) to V-O-based PCMs and evaluated the phase change behavior of disordered and coherent atomic motions evoked by thermal phonons for a given two simulated photon energies ($\hbar w = 1.02$ eV, 1.55 eV) [19]. In addition, other optical/photonic applications on PCMs, such as soft metamaterials and photochemical PCMs, have been reported recently [20,21]. Therefore, ultrashort pulsed lasers could be a better selection to finish the phase change process of PCMs and the physical mechanism should be clarified theoretically and experimentally. Generally, the interaction between laser and solid matter can be categorized into four parts: carrier absorption, thermalization, recombination and structural phase change according to the time evolution [16,22,23]. Femtosecond laser-induced ultrafast melting of PCMs, such as plasma annealing and potential energy surface mutagenesis [17,24], can also complete disordered and ordered phase changes in the cold lattice stage and provide another class of driver for rapid phase changes in optical data storage. Although ultrafast laser-induced phase change is widely clarified in conventional PCMs [18,25,26], it remains largely intractable for the kinetic scenarios and optical excitations triggered by the novel PCMs.

Transition metal composite Sb-Te based phase change alloy as a kind of new PCMs typically exhibit comparable thermal stability and several orders of magnitude faster operation speed with respect to GST [27–30]. In the case of Y-Sb-Te (YST), for example, experiments reveal that the ultralow power consumption is ascribed to the lowered thermal and electrical conductivity of Y, whereas the crystal structure and grain refinement retained by Sb_2Te_3 provide the competitive fast crystallization speed [31,32]. In this work, the amorphization mechanism of YST under photoexcitation is investigated using real-time time-dependant density-functional theory molecular dynamics (rt-TDDFT-MD). The results show that Y-centered motifs in employing strong laser not only maintain its pinning effect, in which also contain undiscovered electronic selective population behavior for the Y-dt_{2g} orbitals. The distorted clusters greatly weaken the short-range Sb-Te structural motifs, resulting in whole rearrange quickly and move out of phase, losing its crystalline order. In this regard, the present work can serve as a valid case demonstrating how the composition of the PCM to be optimized by tuning its amorphization kinetics, aiming at understanding the mechanism by which it results the enhanced high performance phase-change optical memory/computing applications.

II. RESULTS AND DISCUSSION

A. Excited state effects imprinted onto kinetic scenes

The crystalline phase of YST (*c*-YST) material is similar to that of Sb_2Te_3/GST and can be considered as a stable pseudobinary alloy of YTe_2 layered with Sb_2Te_3 as well as a metastable defective rock-salt polycrystal. Similarly, Te occupies the anionic lattice in the supercell, whereas the cation sites are populated by Y, Sb, and 1/3 of the vacancies. Based on the content ratio of the sputtering target, a supercell model
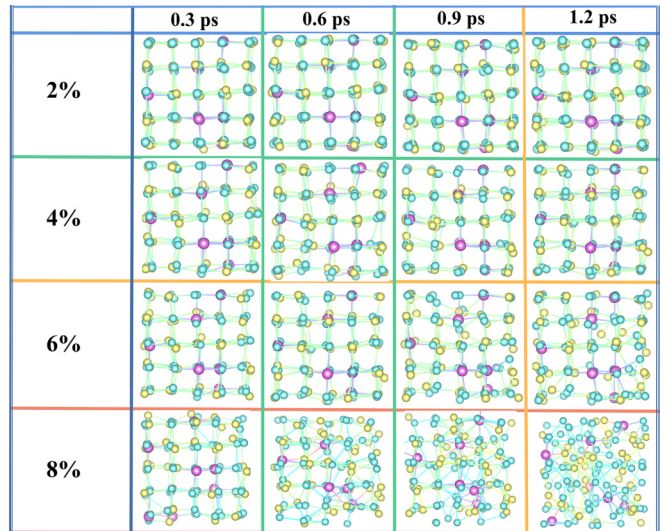

FIG. 1. Structural evolution of Y-Sb-Te displayed in ball-stick fashion upon optical excitation. Snapshots extracted from representative rt-TDDFT-MD trajectories along the out-of-equilibrium dynamics at different optical excitation of valence electrons from 2% to 8% (columns) at 0.3, 0.6, 0.9, and 1.2 ps (rows), respectively. Sb, Te, and Y atoms are represented by yellow, cyan, and pink spheres, respectively.

of $Y_9Sb_{63}Te_{108}$ is constructed and optimized according to the optimum fraction given in the experiment [31]. Details on the structural description are provided in the Appendix B, Fig. 8. It is essential to verify the local structural features of the generated YST (*a*-YST) amorphous model after photoexcitation of 2%, 4%, 6%, and 8% of the valence electrons and performing dynamics for 1.2 ps at the very beginning of 300 K. Figure 1 shows the structural fragments generated during the TDDFT-MD simulation. It can be described in detail as follows: for the case of 2% excitation, the atomic coordination in the octahedral environment exhibits little distortion. In the considered time evolution, there is no sign of disorder in general; For the 4% excitation, the lattice displays a small atomic displacement fluctuation, and the Y atom is firmly pinned to the center while simultaneously appearing distorted in its adjacent lattice. For the 6% excitation, the surrounding sites of Y atoms are strongly distorted and wrong bonds are formed at 0.9 ps. Thus, the lattice is almost unstable, yet the tetragonal ring phase inherent to octahedra can still be observed in large quantities even at 1.2 ps.

Structural snapshots of the 8% excitation are indicative of induced atomic diffusion resulting in extensive bond breakage and loss of crystalline arrangement. Thus, the amorphous model can be obtained at 1.2 ps. Furthermore, structural relaxation of the de-excited state allows recovery of the ground-state electronic conditions, i.e., releasing the excited electrons back to the top of the valence band for further lattice relaxation, thereby removing the role of the force exerted on the atom by electronic excitation. Here, the structural relaxation of the de-excited state verifies that the structure at this moment has fully lost the memory of the original (crystalline) structure (Appendix B, Fig. 9). The transition time for the photoinduced phase change is much lower than the 4.2 and 9
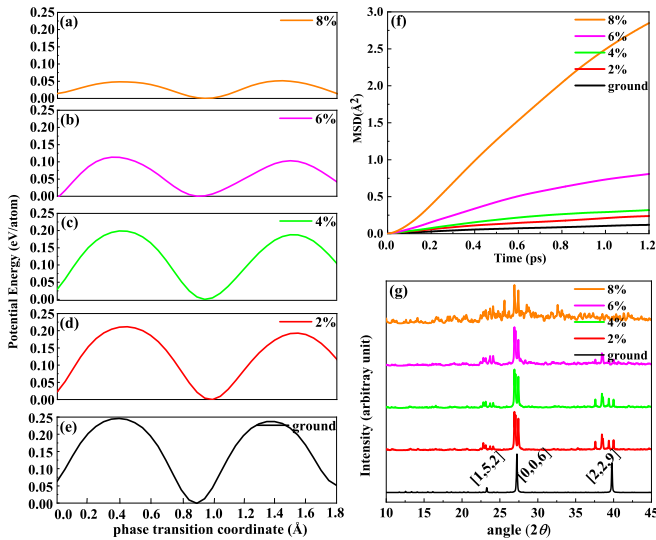
FIG. 2. (a) Potential energy surfaces (PESs) of YST at different photoexcitation levels (b) Mean-square displacement for all the atoms of YST as a function of times upon each excitation. (c) Evolution of simulated diffraction pattern for ground state, 2%, 4%, 6%, and 8% excitations.

ps required for the Sb-Te model and the vacancy-disordered Ge-Sb-Te alloy, respectively, at the same excitation level [25,33]. Hence, the structural changes should have new dynamics beyond homogeneous thermal melting, and the atomic kinetic behavior upon optical excitation differs from that of conventional p-electron forming resonance bonds in PCMs [34].

Optical excitation modifies the potential energy surfaces (PESs), offering an ability to manipulate ordered or disordered phase changes. Such process mediates the force between the atoms and alters the potential energy landscape from that of the ground state, as shown in Figs. 2(a)– 2(e). The PESs flatten out as the excitation increases, whereby the atom can move coherently out of its original phase. Moreover, the alteration of such potential energy landscape along with the effect of coherence forces is well demonstrated both in the femtosecond laser radiation experiments of GeTe, $Ge_2Sb_2Te_5$ and the time-dependent density functional theory [17,18,35]. Hence, the curvature of the potential gets shallower, in which case the position of the atom moves in the photoexcited state, driving the conformational change of the bond. As the excitation continues, the Y-centered motif is subjected to a strong distortion whereby the bonding states are dissociated and even reconfigured. Thus, an 8% sampling excitation can satisfy the amorphous state at 1.2 ps. To shed further light on the excited dynamics responsible for the contrasting results shown in Fig. 1, the mean-square displacement (MSD) is examined for all aforementioned cases. It can be described as

$$\langle R_a^2(t) \rangle = \frac{1}{N_a} \left\langle \sum_{i=1}^{N_a} | R_{ia}(t+\tau) - R_{ia}(\tau) |^2 \right\rangle, \qquad (1)$$

where N_a and R_{ia} denote the total number and coordinates of the i atom, respectively. τ refers to an arbitrary origin of time, taken here as 0. Figure 2(f) illustrates the MSD curves

according to time for all atoms of YST. It can be noticed that the slope of the MSD plot increases as the electronic excited intensity enhances. At ground state, the rock salt structure is in its solid state, and MSD curve is lower than the others. It seems that by 4%, diffusion continues to occur slowly, following tightly the reference curve of the ground state, which means that the structure remains almost unchanged. Comparatively, the pink line in Fig. 2(f), corresponding to the case of 6% excitation, the residual MSD is examined nearly reaching a value of 1 $Å^2$, which is somewhat small yet noticeably higher than that of 4%. Results for 8%, shown by the orange line, the MSD curves is found to be 2.8 $Å^2$, indicative of the amorphous state being satisfied. Therefore, the structure loses its crystalline order and subsequently melts completely in the presence of 8% optical excitation. The calculated electron diffraction pattern of YST over time, Fig. 2(g), provides additional proof about the loss of crystalline order and formation of amorphous ones. In the ground state, there are two strong peaks with angles of 27° and 40° in the [006], [229] planes, and a lower intensity peak in the [152] plane. As the excitation level increases, the strength of the [006] peak remains well defined and is accompanied by splitting(at $t = 1.2$ ps), while the strength of the [229] peak of the crystal structure decreases considerably. Finally, at 8% excitation, one can observe that the intensities of all peaks are diffused. It suggests the full loss of crystalline order and the subsequent formation of amorphous structures.

Next, with the purpose of inspecting the effects on the chemical bonds generated by the excitation, we further evaluate projected crystal orbital Hamiltonian population (pCOHP) that calculates weighted population of wave functions on two atomic orbitals of a pair of adjacent atoms. The calculated -pCOHP is plotted in Fig. 3(a). Although a part of Sb-Te is remained in the antibonding state, yet the excitation does not alter the stable bonding of Y-Te evidently. High excitation leads to the migration of a substantial number of lone-pair and Sb-Te antibonding electrons as well as part of the bonding state electrons from the Y-Te orbitals, thereby causing instability of the crystalline order. Figures 3(b)– 3(e) record the variation of the average coordination number of each atom bonded after the deletion of the valence band electrons as a function of time for different excitation (with a cutoff of 3.2 Å) [36,37]. In the excited initial state (2%–4%), the Y-center still maintain the 6-coordinated octahedrons as a result of thermal effects, while the prevailing defects and the accompanying orderly migration of thermal motions lead to locally changed Sb-, Te-atom coordination environment, whose bonding favors the building of defective octahedra. As we examine the optical excitation terms of 6%–8%, the Y-ligand number increases slowly over time, implying that the excitation preserves both the original coordination of Y-center and facilitates the formation of the small amount of remaining heteropolar Y-Te in the nonoctahedral Y-centered motif. As well, remarkably, there is a noticeable decrease in the Sb-Te coordination number, which provokes us to explore the geometric configuration of the rapid amorphization induced by optical excitation.

Furthermore, chains and rings constitute the essential geometric components for the amorphous and crystalline states of PCMs in the topological space [38–41]. Here, for the first
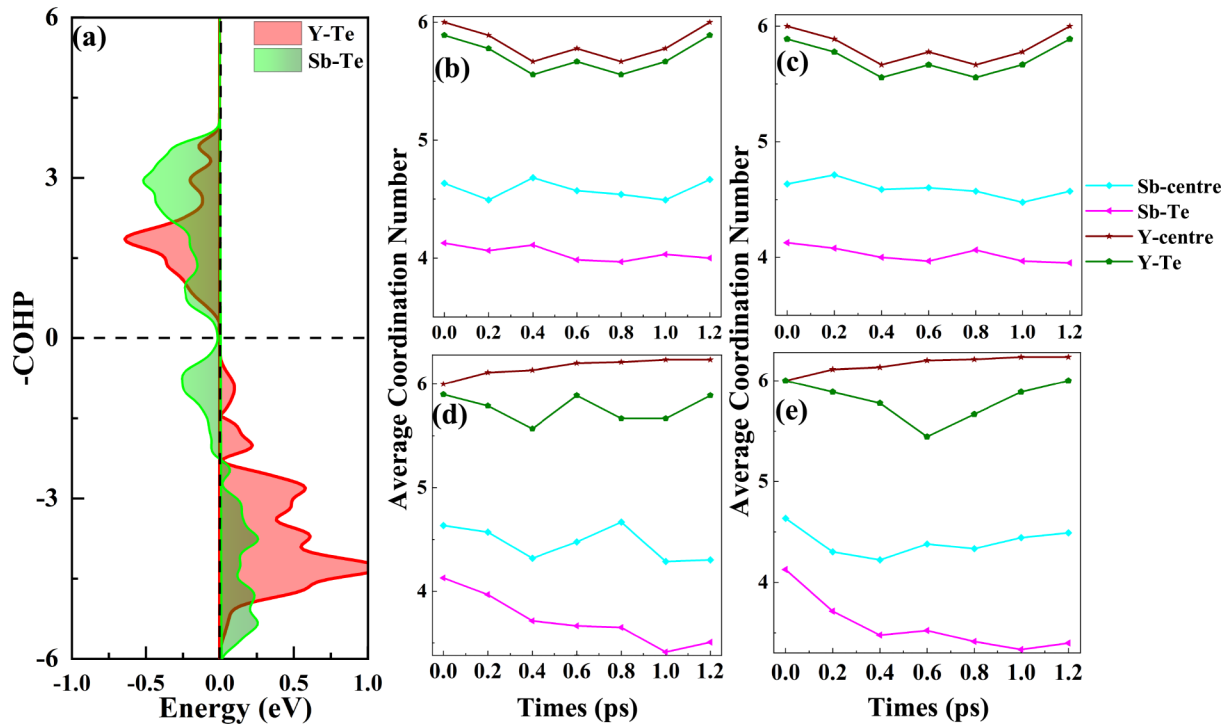
FIG. 3. Optically excited effects on Y-Sb-Te alloys. (a) -pCOHP curves for Y-Te and Sb-Te contact analysis. (b–e) Statistical profiles of the percentage variation of the average coordination number with time at 2%, 4%, 6%, and 8% optical excitation.

time, we investigate the photoinduced evolution of primitive rings as *c*-YST converted to its amorphous phase. As shown in Fig. 4(a), throughout the whole process of excitation, the fourfold rings dominate the ring state. Among them, at 8% excitation, the fraction of threefold rings is second only to the fourfold case, which is similar to the fraction of ring statistics for *a*-Ti-Sb-Te [29]. The majority of the extracted fourfold rings consist mainly of ABAB type, where ABAB squares with A = Y or Sb and B = Te represent the initial units in *a*-YST, and these ring sheets are geometrically deformed upon excitation. Figure 4(b) depicts the typical configuration of the ABAB ring evolving from a normal planar square ring to a warped one. One may conclude that the prevailing defective octahedra may be interrelated via ABAB rings and manifest a tight correlation of fourfold rings and defective octahedra. On the one hand, the above geometrical transformation can be explained by the weak bonding interaction of Sb-Te valence electrons. each Sb, Te atom has three *p* orbitals, p_x, p_y, and p_z, respectively, and each orbital can take up to two electrons. The Sb and Te atoms provide three and four *p*-electrons, respectively, to 3 + 3 = 6 orbitals, which forms six bonds for each atom. According to the electron counting model [42], each orbital is almost only half filled. Therefore, such weakly bonded resonance bonds are susceptible to breakage as well as recombination during the phase change. On the other hand, there is a robust covalent bonding effect in Y-Te, and the typical electronic excitation also modifies the local chemical environment of the Y-center, making the Sb-Te bond of lower stiffness (Appendix C, Fig. 10). As the threshold laser intensity gets strong enough to excite a substantial number of carriers, the coupling strength between the lattice and the carriers is enhanced during energy relaxation, which may steer the system far from equilibrium.

B. Bonding nature and electronic structure of YST at 8% excitation

We now turn to the detailed discussion at 8% excitation. The (partial) pair correlation functions (PCFs) are simulated based on the TDDFT-MD trajectories. Figure 5(a) depicts the pair correlation functions (PCFs) of Sb-Sb, Sb-Te, Y-Sb, Te-Te, and Y-Te pairs in the amorphous. As expected, we find that the Y-Te heteropolar bond is the prevailing first-shell coordination in these bonding motifs. Surprisingly, all of the
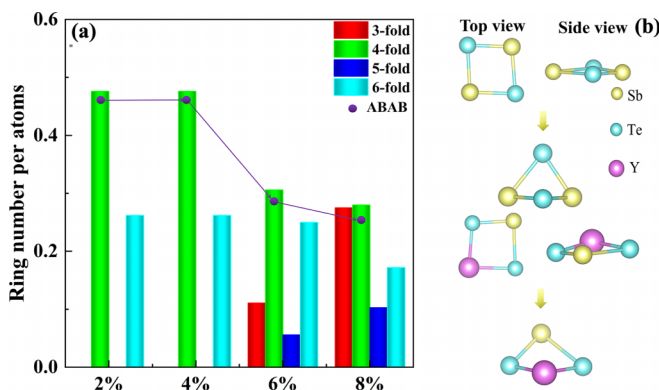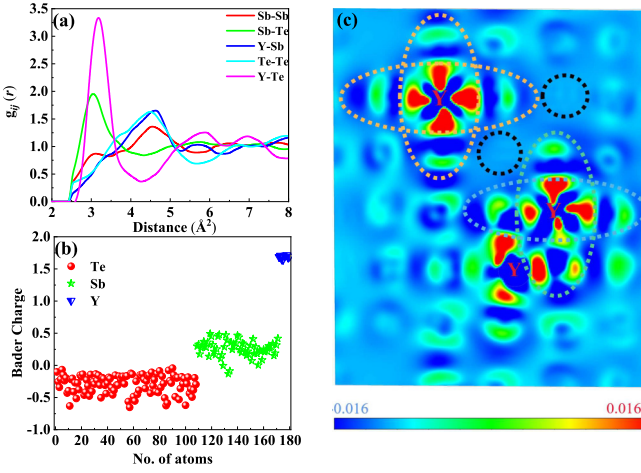

FIG. 4. Ring analysis. (a) The statistics of the primitive ring percentage in different excitation cases, and the circles built into the bar chart represent the proportion of ABAB-type rings within the fourfold ring, where a cutoff of 3.2 Å is used to identify the bonding distance. (b) Sketch of the evolution in fourfold rings.

FIG. 5. (a) The partial pair correlation functions (PCFs) of a-YST models (cutoff at 3.2 Å). (b) The difference in Net Bader charge per component of a-YST between the ground and excited states is quantized. (c) Difference between the self-consistent charge and a superposition of atomic charges (charge density difference, CDD) in a (001) plane for rocksalt YST. Here, CDD is defined as ρ(excited state)-ρ(ground state). In the plot, dashed black circles denote cation vacancies. The ellipse refers to the charge polarization region. Color bar indicates the CDD intensity: red for the positive and blue for the negative intensity. After the excitation, electrons are accumulated around the Y atoms, at the expense of electrons around the Te atoms.
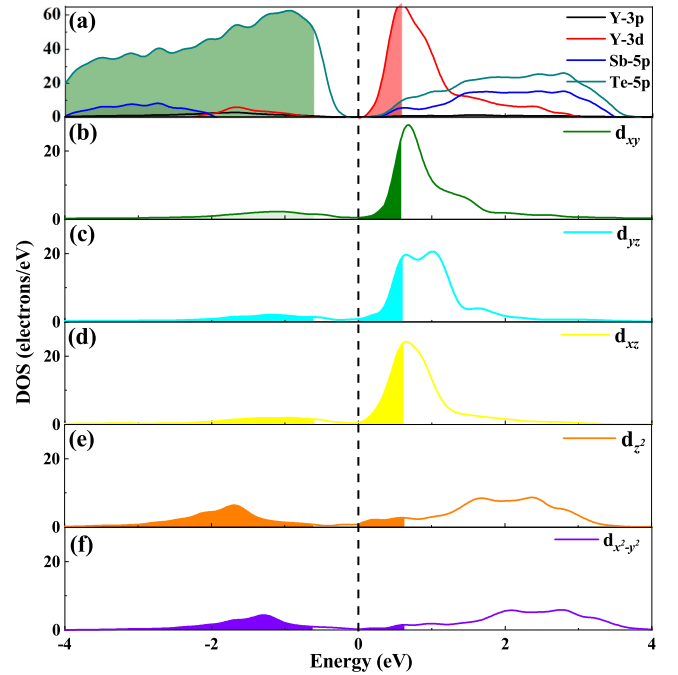

FIG. 6. Orbital-decomposed partial density of states (PDOS) of the Y-Sb-Te alloy. (a) Total PDOS of Y, Sb, and Te. (b–f) The d states of Y decomposed into d_{xy}, d_{yz}, d_{xz} and $d_{x^2-y^2}$, d_{z^2} orbitals, respectively. Partial density of states (PDOS) where electronic occupation upon excitation is shown by color's shading.

homopolar bonds accompanied by their weak first peak almost disappear, which is contrary to that of tremendous homopolar bonds in the common amorphous PCMs [43]. It should be noted that gradual annihilation of other bonds may be ascribed to favorable Y-Te coordination as well as an increase in metallicity leading to a reduction of such defects in the lighter chalcogenides. Such phenomenon arises from the non-negligible charge transfer between the cationlike Sb/Y atoms and the anionlike Te atoms, as indicated by the calculated Net Bader charges for a-YST between the ground and excited states. As shown in Fig. 5(b), each data point corresponds to the charge transfer case of a given atom. The Y-centered motif accepts more electrons compared to Sb, while Te loses most of its electrons in the YST glassy state. It shows that when amorphous Y atoms get more coordination, they capture more electrons at the same time. Moreover, Fig. 5(c) shows the polarization distribution of charge density. The polarization of the electrons propagates in an axial direction along the lattice, as marked by the orange/blue ellipses. We can conclude that electrons reside primarily near Y and its surrounding Te. In other words, the electrons are excited and pumped into specific orbitals of Y. Excitation is essentially an event of selective transport from anions to cations.

To clarify the explicit path of optical excitation, we perform the orbital-resolved partial density of states (PDOS) of YST by the first-principles calculations. The total and partial density of states from the calculations are shown in Figs. 6(a)–6(f). In general, a broad Te/Sb-p-Y-d hybridized-state band extending towards the Fermi level. In the valence band region, the Te-p state is predominant, whereas Y-d states make the greatest contribution over that of Sb/Te-p states to this

bottommost conduction band. Normally, the rule for electron occupancy follows the Fermi-Dirac distribution at thermal equilibrium conditions (Appendix D, Fig. 11). In the presence of crystal field effect, when the ligand (Sb$_2$Te$_3$) forms an orthoctahedron with Y-atom whose angle of the d-orbital electron cloud owns a high resolution, the d orbital will encounter a large repulsive effect and be induced to split into, a higher energy level t_{2g} and a lower energy level e_g. According to the dipole selection rule, the transition probability depends on the geometry of the orbitals, i.e., $M_{ij} = \langle \psi_j \mid \hat{r} \mid \psi_i \rangle$, where M_{ij} is the transition matrix element between the initial Bloch state ψ_i and final Bloch state ψ_j. We identify $\langle d_{xy} \mid \hat{r} \mid p \rangle$, $\langle d_{yz} \mid \hat{r} \mid p \rangle$, $\langle d_{xz} \mid \hat{r} \mid p \rangle$ as the three main transition paths in the excitation event, while the transition paths of $\langle d_{z^2} \mid \hat{r} \mid p \rangle$, $\langle d_{x^2-y^2} \mid \hat{r} \mid p \rangle$ are suppressed as a result of crystal field effects. As can be seen, Figs. 6(b)– 6(f) depict that the d_{xy}, d_{yz}, and d_{xz} orbitals show the dominant state occupation prior to the $d_{x^2-y^2}$ and d_{z^2} orbitals.

Since the p-electron excitation possesses a well-defined d-orbital selectivity, the change of the Y-centered bond angle during the ultrafast phase change is inevitably obeyed by the angle orientation of the conduction band bottom e_g and t_{2g} hybrid orbitals. To verify our hypothesis, the bond angle distributions of e_g, t_{2g}, and e_g hybrid with t_{2g} were plotted as shown in Figs. 7(a)– 7(c). Combined with the analysis of the PDOS, it is clear that the e_g form hybridized states with Te-p in the valence band for bonding, while $d_{x^2-y^2}$ can form 90° and 180° with d_{z^2} in the way of electron cloud angle. Thus, the Y-centered bond angles are ideally 90° and 180° in the c-YST. Here, the initial bond angle is subject to deviation as a result
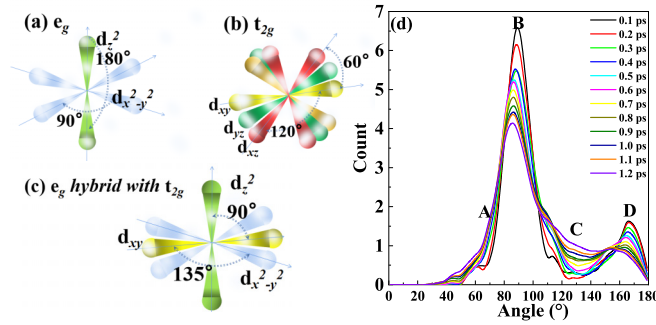
FIG. 7. Bonding motif of the Y-center configuration at 8% excitation. (a) The electron clouds of e_g orbitals are distributed with 90° and 180° as the signature of c-YST bond angles, respectively. (b) The electron clouds of t_{2g} orbitals are allocated with a type angle of 60° and 120°, respectively. (c) The hybridized orbitals cause the initial angle of the electron cloud to be favored by 90° and 135°. (d) Time evolution of bond angle distribution of Y-centered upon excitation.

of the random presence of defects and thermal vibration, as shown in Fig. 7(d). In Fig. 7(b), the t_{2g} orbitals d_{yz}, d_{xz}, d_{xy} can perform 60° and 120° in two, so the bond angles following hybridization [Fig. 7(c)] can be distinguished into two parts, i.e., 135° and 90° formed when coplanar and noncoplanar. Then, we calculated the time-dependent evolution of the Y-centered bond angle upon excitation, and it can be seen that the 90°, peak B, shifted gradually to the left over time and is coupled with an increase of counts for the 70°, labeled as A, while the original 170°, peak D, move to the left and is associated with the increase of counts for the 130°, labeled as C. Therefore, it can qualitatively consider that the actual increase of 70° and 130° angles is a reminiscence of the 60° and 135° angles in Figs. 7(b) and 7(c), respectively. To highlight the unique role of electronic excitation, we perform a comparative analysis of the Y-centered bond angle distribution driven by purely thermal effects, and as a result, the primary angle of 90° is well retained. See details in the Appendix D, Fig. 12(b). Thus, the essence of the ultrafast amorphization induced by excitation is actually the rapid evolution of the Y-centered bond angle, which gives rise to changes in the atomic coordination number and ring statistics.

III. CONCLUSION AND OUTLOOK

In summary, we obtain the a-YST model dissociation with optical excitations in rt-TDDFT-MD simulations. The results show that photoinduced YST undergoes an inhomogeneous and local ultrafast disordering in which all the degrees of freedom are excited simultaneously. The photoinduced amorphization process can be elucidated concisely as follows: the low concentration of photoexcitation cannot conquer the potential barrier to allow the atoms out of the original phase, but rather proceeds to a stable thermal vibration and fails to undergo a phase transition. At 8% excitation, a considerable number of optically extracted electrons selectively occupy the t_{2g} orbitals, which leads to a hybrid of Y-centered bond angles toward the e_g and t_{2g} hybrid orbitals, resulting in irreversible separation of the atoms from their original phase and loss of the crystalline order. This work provides an time-efficient

pathway for rapid amorphization in the form of extending photoexcitation to other similar transition metal alloyed PCMs to achieve the desired phase change response speed.

APPENDIX A: MATERIALS AND METHODS

We perform the rt-TDDFT-MD simulations based on the norm-conserving pseudopotentials (NCPP) and PBE exchange-correlation functional, which is implemented in the code PWmat [44–46]. To leap over the efficiency barrier stemming from the extremely tiny time step demands of the conventional TDDFT algorithm [47–49], the time-dependent Kohn-Sham's single-particle equation is

$$i \frac{\partial \psi_j(t)}{\partial t} = H[\rho(t)]\psi_j(t), \tag{A1}$$

the time-dependent wave function $\psi_j(t)$ is prolonged by the adiabatic eigenstate $\phi_i(t)$

$$\psi_j(t) = \sum_i C_{j,i}(t)\phi_i(t), \tag{A2}$$

$$H(t)\phi_i(t) = \epsilon_i(t)\phi_i(t). \tag{A3}$$

Here, $H(t) \equiv H(t, R(t), \rho(t))$, $R(t)$ refers to the nuclear positions, and $\rho(t)$ stands for the charge density. From Eqs. (A2) and (A3) we get

$$\dot{C}_{j,i}(t) = -i\epsilon_i(t)C_{j,i}(t) - \sum_l C_{j,l}(t)V_{i,l}(t), \tag{A4}$$

where the transition matrix $V_{i,l}(t) = \langle \phi_i(t) \mid \partial\phi_l(t)/\partial t \rangle$. Since a finite number of adiabatic states $\phi_i(t)$ are determined in the expansion of Eq. (A3), thus, the aforesaid procedure can transform the initial problems into the small-size matrix ones of Eq. (A5). In Eq. (A4), a linear-time-dependent Hamiltonian (LTDH) is employed to denote the time-dependence of the Hamiltonian over a time step. More precisely, for a time interval $[t_1, t_1 + \Delta t]$, the eigenstates at $t_1\{\psi_l(t_1)\}$ are employed as the basis set to expand the Hamiltonian equations. The Hamiltonian at t_1 contains only the diagonal term $\{\varepsilon_l(t_1)\}$, whereas it is diagonal at the basis set $\{\psi_l(t_1 + \Delta t)\}$ of $t_1 + \Delta t$. It can be assumed that the Hamiltonian evolves in a linear fashion over $[t_1, t_1 + \Delta t]$. For any $t \in [t_1, t_1 + \Delta t]$,

$$H(t) = H(t_1) + \frac{t - t_1}{\Delta t}[H(t_1 + \Delta t) - H(t_1)]. \tag{A5}$$

With the adiabatic eigenstate basis set, the linear approximation of Hamiltonian allows a well-defined description of the real $H(t)(\Delta t \leqslant 0.2$ fs$)$, which is several orders of magnitude longer than the time step of 1 as in the conventional rt-TDDFT [46,50]. The plane wave energy cutoff is 50 Ry and the time step is fixed to 0.1 fs in our calculation. The equilibrium state of *ab initio* MD at 300 K is adopted as the input to rt-TDDFT. Based on this structure, we then utilize the rt-TDDFT algorithm to simulate the time evolution of Y-Sb-Te upon excitation. In both *ab initio* MD and rt-TDDFT-MD, we use a 180-atom supercell for rock-salt Y-Sb-Te and the Γ point for Brillouin zone sampling. Initial excitation is performed by removing electrons from HOMO to HOMO+n bands and placing them in LUMO to LUMO+n bands, where n is the number of excited bands. The number of excited electrons is twice the number of the band to which it corresponds. The excitation intensity is presented as a percentage of the total number of valence electrons. According to the pseudopotential employed in this work, Y, Sb, and Te have 3, 5, and 6 valence electrons, respectively. Thus, the calculated model contains a total of 990 valence electrons. The various excitations (2%, 4%, 6%, and 8% in Fig. 1) are realized by manipulating the number of total valence electrons shifting to the conduction band. In the case of 8% excitation, for example, about 80 electrons near the top of the valence band are moved to the bottom of the conduction band.

Here, we utilize a 250 nm pulsed laser to pump the electrons. As for the 250 nm laser pulse, the total energy is $\hbar\omega_o = 4.78$ eV$(\omega_o = 2\pi c/\lambda)$, considerably higher than the band gap of 0.25 eV in the case of $Y_{0.25}Sb_{1.75}Te_3$ [51]. Consequently, we would consider linear absorption directly. The calculation of the excited electron-hole plasma concentration N_{e-h} is expressed as follows:

$$N_{e-h} = (1-R)\frac{\alpha_{\text{eff}}F}{\hbar\omega_o}, \tag{A6}$$

where R refers to the reflectivity, α_{eff} is derived from the effective absorption coefficient of the dopant, and F and $\hbar\omega_o$ denote the laser fluence and frequency, respectively. For 8% excitation, the calculated fluence is 23.2 mJ/cm^2 and the total energy density desired for amorphization is 23.2 mJ/cm^3. Calculation of simplified laser-induced excited states has been correctly verified on the basis of experiment and theory [52–54]. Crystal orbital Hamilton populations (COHP), as well as chemical bonding analysis, are computed using LOBSTER within the framework of DFT wave functions [55,56]. The trajectory of rt-TDDFT-MD simulation is further investigated using rigorous investigation of networks generated simulations (R.I.N.G.S.) code to obtain statistics of primitive rings and coordination number [57,58].

APPENDIX B: STRUCTURAL DESCRIPTION AND ROLE OF DE-EXCITED

We first construct a NaCl-type cubic Sb_2Te_3 supercell whose density is taken from the experimentally determined density [59]. Then, some of the Sb atoms are substituted with Y atoms according to the experimentally optimal component ratio, and the final supercell component $Y_9Sb_{63}Te_{108}$ (abbreviated as YST in the paper) is shown in Fig. 8(a). Next,
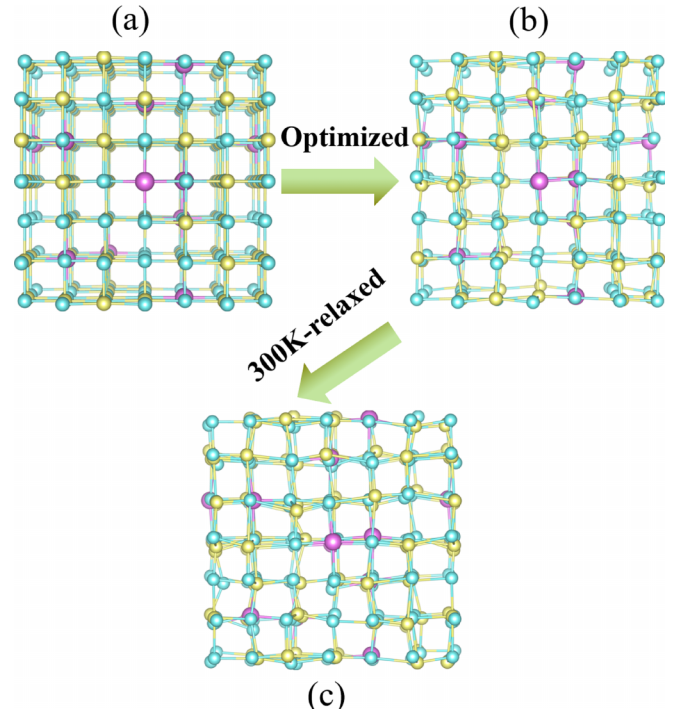

FIG. 8. Simulated supercell structure of $Y_{0.25}Sb_{1.75}Te_3$ (a) after optimization (b) and 300K relaxation (c), respectively. Color coding: yellow, cyan, and pink spheres correspond to Sb, Te, and Y atoms, respectively.

we optimized the supercell carefully to obtain a theoretically reasonable structure with lattice constants of a = 18.8952 Å, b = 19.7609 Å, c = 19.5280 Å, $\alpha = 88.7017°$, $\beta = 90.0910°$, and $\gamma = 90.1028°$, as shown in Fig. 8(b). Note that the optimized lattice parameters here are slightly larger than those of Sc-Sb-Te, because when Y and Sc are doped into the Sb_2Te_3 lattice separately, the former expands the lattice while the latter shrinks it [27,60]. Finally, we equilibrated the optimized structure at 300 K for 3 ps to get the initial input structure of rt-TDDFT-MD, as shown in Fig. 8(c).

To examine whether the amorphization of YST is realized, the structural optimization of the fragment of TDDFT-MD with de-excitation is rather essential. As shown in Fig. 9, YST is gradually disordered after 1.2 ps at 6% excitation. Nevertheless, these structures turn back into the crystalline phase after optimization. On the contrary, after 1.2 ps of 8% excitation, the structures are still manifestly disordered even after careful optimization, which suggests that the structures have lost the memory of the crystalline phase intact. In contrast, the 8% excitation is still accompanied by a fourfold cubes residue of the crystalline phase after 0.9 ps.

APPENDIX C: ADJACENCY-RETENTION FUNCTION AND -ICOHP

To dissect the dynamic law between the structural evolution and its bonding strength upon optical excitation, we define an (average) primordial adjacency-retention function $A(t)$, which recalls how many primal adjacency Te atoms are
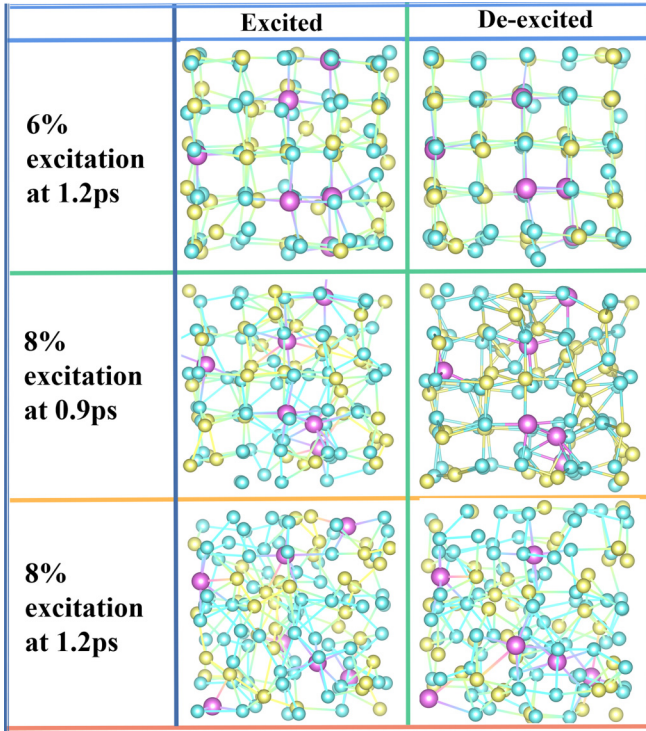
FIG. 9. Structures of the 6% excitation at 1.2 ps, the 8% excitation at 0.9 ps, and the 8% excitation for 1.2 ps of Y-Sb-Te(collected in MD) before and after the de-excited structural optimization.

FIG. 11. Partial density of states (PDOS) for the orbital decomposition of Y-Sb-Te alloys without excitation. (a) Total PDOS for Y, Sb, and Te. (b–f) The d states of Y decomposed into d_{yz}, d_{xz}, d_{xy} and $d_{x^2-y^2}$, d_{z^2} orbitals, respectively, with electron occupancy in the PDOS indicated by shading of colors.

retained by a cation during the amorphization process:

$$A(t) = \frac{1}{n} \sum_{j=1}^{n} \frac{N_{jt}}{N_{j0}}. \qquad (C1)$$

n refers to the number of cations (Y or Sb) to be collected, where N_{j0} is the number of primitive neighbors and N_{jt} is the number of reservations at time t. As shown in Fig. 10(a), at 8% excitation, the $A(t)$ profile of the Y atom possesses a much slower decrease than that of the Sb one, moreover, by
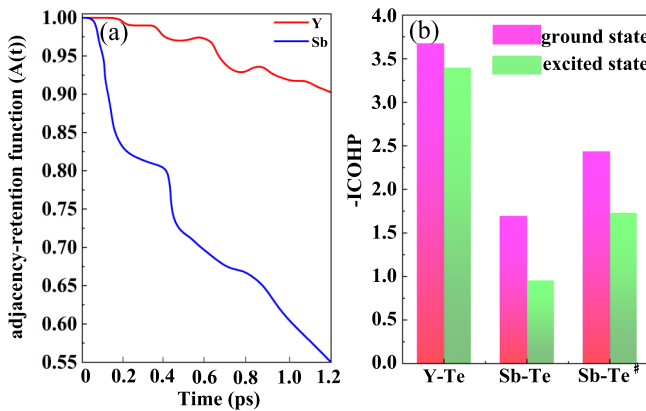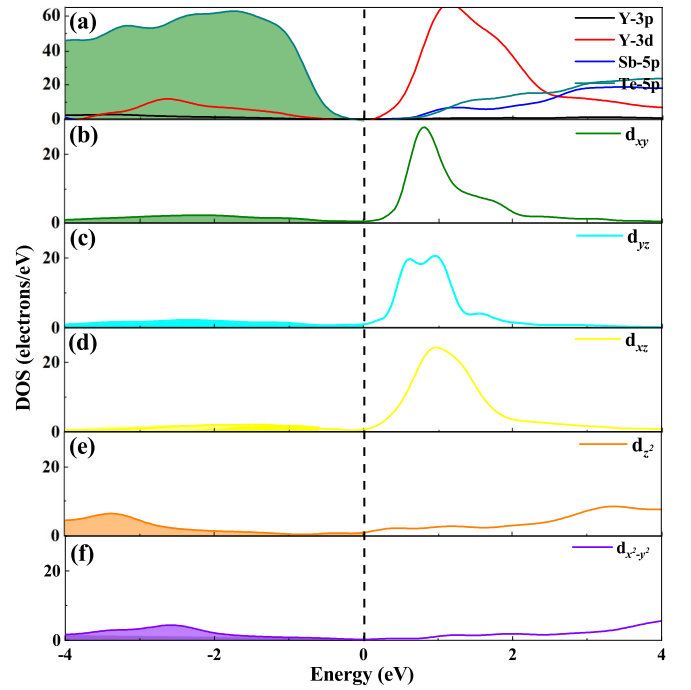

FIG. 10. (a) Temporal evolution of the (average) primordial adjacency-retention function $A(t)$ during amorphization upon 8% excitation (cutoff at 3.2 Å). (b) Integrated Crystal orbital Hamilton populations (-ICOHP) for Y-Te, Sb-Te bonds (clustered around the Y networks) and Sb-Te$^{\sharp}$ (not next to Y networks).

the end of the simulation it still maintains a 90% contribution, while the retention fraction of Sb drops to 55%. The disparity in the number of adjacency-retention of the two cations implies an extensive breakage of the Sb surrounding bonds during the photoexcitation, while Y is more favorable for the formation of superatomic cluster centers. Furthermore, the resulting COHP curve constitutes an electron number allocating plan that allow the use of its integral up to the Fermi level (ICOHP) as a quantization index of bond strength, as shown in Fig. 10(b). Normally, a negative correlation exists between the ICOHP value and the strength of the interaction. That is, a larger absolute value of the negative ICOHP leads to a stronger bonding coupling. The -ICOHP values for the bonds of Y-Te and Sb-Te (next to the Y-Te bonds) at the ground states are 3.7 and 1.7, respectively. Whereas, at the 8% excitation, the Sb-Te bond strength has been notably weakened, with a reduction of about 47%. In addition, the excited state of -ICOHP shows Sb-Te$^{\sharp}$ bonds, which are not in the Y-adjacent lattice, further make the bond of lower stiffness. Meanwhile, the -ICOHP results confirm that Y-centered clusters possess strong bonding environment with Te in both the ground and excited states.

APPENDIX D: THERMAL EQUILIBRIUM STATE

From Fig. 11, the e_g and t_{2g} orbitals occupy the higher and lower energy windows of the conduction band, respectively, with the dominant effect of the crystal field. In contrast to the density of states obtained from the transient ground-locked
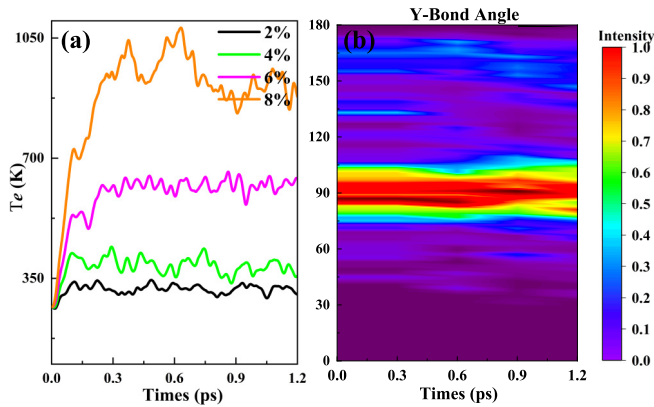
FIG. 12. (a) Temperature change over time at differently applied electronic excitations (t_e) and (b) the distribution of Y-centered bond angles and their evolution without excitation (Melt-quenching). The color bar denotes normalized intensity: strong and weak intensity are displayed in red and blue, respectively.

electron population, the valence band electrons of the thermal equilibrium state will follow the Fermi-Dirac distribution and occupy the valence band region extensively. By extracting the time-dependent electronic excited temperature (t_e), the sharp increase in ion temperature is ascribed to the great driving force on the atom induced by optical excitation, as shown in Fig. 12(a). The ion temperature is a statistic of the kinetic energy (E) of each atom, i.e., $3\kappa_B t/2 = E$, where κ_B is the Boltzmann constant and T is the absolute temperature. In the case of ultrafast excitations, the ion temperature of rt-TDDFT-MD refers to the nominal transient temperature rather than the standard thermal temperature at equilibrium. For comparison, we perform the evolution of the Y-centered bond angle based on the pre-melting process, it was quickly heated above t_e (1050K), equilibrated for another 6 ps. Note that the data were collected based on a last 1.2 ps of *ab initio* MD trajectories. It can be seen from Fig. 12(b) that in the situation without excitation, the moderate shift toward higher or lower angles deviate from 90° bond angles is due to more Y atoms becoming associated with Te atoms in octahedral coordination and the hybridization of d/s and p orbitals or presence of cation vacancies. Thus, the photoinduced phase change has an essential difference beyond the homogeneous change.

[1] W. Zhang, R. Mazzarello, M. Wuttig, and E. Ma, Nat. Rev. Mater. **4**, 150 (2019).

[2] P. Yao, H. Wu, B. Gao, J. Tang, Q. Zhang, W. Zhang, J. J. Yang, and H. Qian, Nature (London) **577**, 641 (2020).

[3] J. Feldmann, N. Youngblood, C. D. Wright, H. Bhaskaran, and W. H. P. Pernice, Nature (London) **569**, 208 (2019).

[4] S. J. Gong, C. Gong, Y. Y. Sun, W. Y. Tong, C. G. Duan, J. H. Chu, and X. Zhang, Proc. Natl. Acad. Sci. USA **115**, 8511 (2018).

[5] C. Qiao, K. Bai, M. Xu, S. Wang, C. Z. Wang, K. M. Ho, X. Miao, and M. Xu, Acta Mater. **216**, 117123 (2021).

[6] Y. T. Liu, X. B. Li, H. Zheng, N. K. Chen, X. P. Wang, X. L. Zhang, H. B. Sun, and S. Zhang, Adv. Funct. Mater. **31**, 2009803 (2021).

[7] B. Huang and J. Robertson, Phys. Rev. B **81**, 081204(R) (2010).

[8] N. Y. Matthias, Nat. Mater. **6**, 824 (2007).

[9] R. O. Jones, Phys. Rev. B **101**, 024103 (2020).

[10] S. M. Islam, L. Peng, L. Zeng, C. D. Malliakas, D. Y. Chung, D. B. Buchholz, T. Chasapis, R. Li, K. Chrissafis, J. E. Medvedeva, G. G. Trimarchi, M. Grayson, T. J. Marks, M. J. Bedzyk, R. P. H. Chang, V. P. Dravid, and M. G. Kanatzidis, J. Am. Chem. Soc. **140**, 9261 (2018).

[11] M. H. R. Lankhorst, L. V. Rieterson, M. V. Schijndel, B. A. J. Jacobs, and J. C. N. Rijpers, Jpn. J. Appl. Phys. **42**, 863 (2003).

[12] Y. Cheng, X. Han, and X. Liu, Appl. Phys. Lett. **93**, 183113 (2008).

[13] Y. M. Chen, J. R. Gu, Q. Zhang, Y. E. Mao, G. X. Wang, R. P. Wang, X. Shen, J. Q. Wang, and T. F. Xu, Phys. Rev. Mater. **4**, 033403 (2020).

[14] C. Peng, Z. T. Song, and F. Rao, Appl. Phys. Lett. **99**, 043105 (2011).

[15] K. Sugioka and Y. Cheng, Light Sci. Appl. **3**, e149 (2014).

[16] S. K. Sundaram and E. Mazur, Nat. Mater. **1**, 217 (2002).

[17] N. K. Chen, X. B. Li, J. Bang, X. P. Wang, D. Han, D. West, S. Zhang, and H. B. Sun, Phys. Rev. Lett. **120**, 185701 (2018).

[18] E. Matsubara, S. Okada, T. Ichitsubo, T. Kawaguchi, A. Hirata, P. F. Guan, K. Tokuda, K. Tanimura, T. Matsunaga, M. W. Chen, and N. Yamada, Phys. Rev. Lett. **117**, 135501 (2016).

[19] H. W. Liu, W. H. Liu, Z. J. Suo, Z. Wang, J. W. Luo, S. S. Li, and L. W. Wang, Proc. Natl. Acad. Sci. USA **119**, e2122534119 (2022).

[20] Q. Wang, E. T. F. Rogers, B. Gholipour, C. M. Wang, G. Yuan, J. Teng, and N. I. Zheludev, Nat. Photon. **10**, 60 (2016).

[21] S. Wu, T. Li, Z. Y. Zhang, T. Li, and R. Wang, Matter **4**, 3385 (2021).

[22] R. H. Groeneveld, R. Sprik, and A. Lagendijk, Phys. Rev. B: Condens. Matter **51**, 11433 (1995).

[23] J. Zhang, C. Lian, M. X. Guan, W. Ma, H. X. Fu, H. Z. Guo, and S. Meng, Nano Lett. **19**, 6027 (2019).

[24] J. Bang, Y. Y. Sun, X. Q. Liu, F. Gao, and S. B. Zhang, Phys. Rev. Lett. **117**, 126402 (2016).

[25] X. B. Li, X. Q. Liu, X. Liu, D. Han, Z. Zhang, X. D. Han, H. B. Sun, and S. B. Zhang, Phys. Rev. Lett. **107**, 015501 (2011).

[26] P. Fons, H. Osawa, A. V. Kolobov, T. Fukaya, M. Suzuki, T. Uruga, N. Kawamura, H. Tanida, and J. Tominaga, Phys. Rev. B **82**, 041203(R) (2010).

[27] S. W. Hu, J. K. Xiao, J. Zhou, S. R. Elliott, and Z. M. Sun, J. Mater. Chem. C **8**, 6672 (2020).

[28] Y. Wang, T. Guo, G. Liu, T. Li, S. Lv, S. Song, Y. Cheng, W. Song, K. Ren, and Z. Song, ACS Appl. Mater. Interface **11**, 10848 (2019).

[29] M. Zhu, M. Xia, F. Rao, X. Li, L. Wu, X. Ji, S. Lv, Z. Song, S. Feng, H. Sun, and S. Zhang, Nat. Commun. **5**, 4086 (2014).

[30] F. Rao, Z. Song, Y. Cheng, X. Liu, M. Xia, W. Li, K. Ding, X. Feng, M. Zhu, and S. Feng, Nat. Commun. **6**, 10040 (2015).

[31] B. Liu, W. Liu, Z. Li, K. Li, L. Wu, J. Zhou, Z. Song, and Z. Sun, ACS Appl. Mater. Interface **12**, 20672 (2020).

[32] B. Liu, K. Q. Li, W. L. Liu, J. Zhou, L. C. Wu, Z. T. Song, S. R. Elliott, and Z. M. Sun, Sci. Bull. **66**, 2217 (2021).

[33] S. C. Tiwari, R. K. Kalia, A. Nakano, F. Shimojo, P. Vashishta, and P. S. Branicio, J. Phys. Chem. Lett. **11**, 10242 (2020).

[34] X. P. Wang, X. B. Li, N. K. Chen, Q. D. Chen, X. D. Han, S. B. Zhang, and H. B. Sun, Acta Mater. **136**, 242 (2017).

[35] J. Hu, G. M. Vanacore, Z. Yang, X. Miao, and A. H. Zewail, ACS Nano **9**, 6728 (2015).

[36] C. Qiao, Y. R. Guo, S. Y. Wang, M. Xu, X. S. Miao, C. Z. Wang, and K. M. Ho, Appl. Phys. Lett. **114**, 071901 (2019).

[37] T. Matsunaga, J. Akola, S. Kohara, T. Honma, K. Kobayashi, E. Ikenaga, R. O. Jones, N. Yamada, M. Takata, and R. Kojima, Nat. Mater. **10**, 129 (2011).

[38] M. Micoulaut, A. Kachmar, M. Bauchy, S. LeRoux, C. Massobrio, and M. Boero, Phys. Rev. B **88**, 054203 (2013).

[39] J. Akola and R. O. Jones, J. Phys. Condens. Matter. **20**, 465103 (2008).

[40] S. Caravati, M. Bernasconi, T. D. Kuhne, M. Krack, and M. Parrinello, Phys. Rev. Lett. **102**, 205502 (2009).

[41] S. Kohara, K. Kato, S. Kimura, H. Tanaka, T. Usuki, K. Suzuya, H. Tanaka, Y. Moritomo, T. Matsunaga, N. Yamada, Y. Tanaka, H. Suematsu, and M. Takata, Appl. Phys. Lett. **89**, 201910 (2006).

[42] L. X. Zhang, E. G. Wang, Q. K. Xue, S. B. Zhang, and Z. Y. Zhang, Phys. Rev. Lett. **97**, 126103 (2006).

[43] D. V. Bochek, N. S. Solodovchenko, D. A. Yavsin, A. B. Pevtsov, K. B. Samusev, and M. F. Limonov, Phys. Rev. B **105**, 165425 (2022).

[44] W. L. Jia, J. Lang, X. B. Chi, and L. W. Wang, Comput. Phys. Commun. **211**, 8 (2017).

[45] W. H. Liu, J. W. Luo, S. S. Li, and L. W. Wang, Phys. Rev. B **102**, 184308 (2020).

[46] Z. Wang, S. S. Li, and L. W. Wang, Phys. Rev. Lett. **114**, 063004 (2015).

[47] A. Marini, C. Hogan, M. Grning, and D. Varsano, Comput. Phys. Commun. **180**, 1392 (2009).

[48] X. Andrade, J. A. Rodriguez, D. A. Strubbe, M. J. T. Oliveira, F. Nogueira, and A. Castro, J. Phys. Condens. Matter. **24**, 233202 (2012).

[49] G. Kolesov, O. Granas, R. Hoyt, D. Vinichenko, and E. Kaxiras, J Chem. Theory. Comput. **12**, 466 (2016).

[50] J. Ren, N. Vukmirovic, and L. W. Wang, Phys. Rev. B **87**, 205117 (2013).

[51] Z. Li, C. Si, J. Zhou, H. Xu, and Z. Sun, ACS Appl. Mater. Interfaces **8**, 26126 (2016).

[52] X. B. Li, X. Q. Liu, and X. D. Han, Phys. Status Solidi B **249**, 1861 (2012).

[53] S. Wall, S. Yang, L. Vidas, M. Chollet, J. M. Glownia, M. Kozina, T. Katayama, T. Henighan, M. Jiang, T. A. Miller, D. A. Reis, L. A. Boatner, O. Delaire, and M. Trigo, Science **362**, 572 (2018).

[54] N. K. Chen, J. Bang, X. B. Li, X. P. Wang, D. Wang, Q. D. Chen, H. B. Sun, and S. B. Zhang, Phys. Rev. B **102**, 184115 (2020).

[55] S. Maintz, V. L. Deringer, A. L. Tchougreeff, and R. Dronskowski, J. Comput. Chem. **34**, 2557 (2013).

[56] S. Maintz, V. L. Deringer, A. L. Tchougreeff, and R. Dronskowski, J. Comput. Chem. **37**, 1030 (2016).

[57] X. Yuan and A. N. Cormack, Comput. Mater. Sci. **24**, 343 (2002).

[58] S. L. Roux and P. Jund, Comput. Mater. Sci. **49**, 70 (2010).

[59] Y. H. Zheng, M. J. Xia, Y. Cheng, F. Rao, K. Y. Ding, W. L. Liu, J. Yu, Z. T. Song, and S. L. Feng, Nano Res. **9**, 3453 (2016).

[60] F. Rao, K. Ding, Y. Zhou, Y. Zheng, M. Xia, S. Lv, Z. Song, S. Feng, I. Ronneberger, R. Mazzarello, W. Zhang, and E. Ma, Science **358**, 1423 (2017).